Data-driven simulation of rapid flux enhancement of energetic electrons with an upper-band whistler burst

S. Saito[1], S. Kurita[2], Y. Miyoshi[3], S. Kasahara[4], S. Yokota[5], K. Keika[4], T. Hori[3], Y. Kasahara[6], S. Matsuda[7], M. Shoji[3], S. Nakamura[3], A. Matsuoka[8], S. Imajo[3], I. Shinohara[7]

[1]Space Environment Laboratory, Applied Electromagnetic Research Institute, National Institute of Information and Communications Technology, Tokyo, Japan
[2]Research Institute for Sustainable Humanosphere, Kyoto University, Uji, Japan
[3]Institute for Space-Earth Environmental Research, Nagoya University, Nagoya, Japan
[4]Graduate School of Science, University of Tokyo, Tokyo, Japan
[5]Graduate School of Science, Osaka University, Toyonaka, Japan
[6]Graduate School of Natural Science and Technology, Kanazawa University
[7]Institute of Space and Astronautical Science, Japan Aerospace Exploration Agency, Kanagawa, Japan
[8]Graduate School of Science, Kyoto University, Kyoto, Japan

Key Points:

- The data-driven simulation of rapid flux enhancement has been performed using plasma/particle and wave data obtained by Arase.
- The simulation results reproduce the observed temporal variations of energetic electron flux distributions.
- The nonlinear phase trapping contributes to the flux enhancement of electrons above 20 keV.

Corresponding author: Shinji Saito, s.saito@nict.go.jp

Abstract

The temporal variation of the energetic electron flux distribution caused by whistler mode chorus waves through the cyclotron resonant interaction provides crucial information on how electrons are accelerated in the Earth's inner magnetosphere. This study employing a data-driven test-particle simulation demonstrates that the rapid deformation of energetic electron distribution observed by the Arase satellite is not simply explained by a quasi-linear diffusion mechanism, but is essentially caused by nonlinear scattering: the phase trapping and the phase dislocation. In response to upper-band whistler chorus bursts, multiple nonlinear interactions finally achieve an efficient flux enhancement of electrons on a time scale of the chorus burst. A quasi-linear diffusion model tends to underestimate the flux enhancement of energetic electrons as compared with a model based on the realistic dynamic frequency spectrum of whistler waves. It is concluded that the nonlinear phase trapping plays an important role in the rapid flux enhancement of energetic electrons observed by Arase.

Plain Language Summary

Energetic electrons could be a cause of satellite anomalies affected by electric discharge phenomena on its surface and interior materials. To minimize the anomalies through satellite operation, it is important to forecast the temporal variation of the energetic electron flux along the trajectories of a satellite. One of the causes of the variation of the electron flux is whistler mode waves, which are right-handed, circularly polarized electromagnetic waves that can resonate with energetic electrons. To understand how the electrons are accelerated in realistic situations, we have performed a data-driven numerical simulation to demonstrate electron scattering, by importing the observation data of the Arase satellite directly to the simulation. Results of the simulation reproduce the temporal variations of energetic electron flux distributions in burst of whistler mode waves. It is found that the nonlinear scattering contributes to the flux enhancement of energetic electrons. It is confirmed that a quasi-linear diffusion model, which has been used in general so far, cannot explain such a rapid flux enhancement. We conclude that the nonlinear scattering caused by the whistler burst plays an important role in the rapid flux enhancement of energetic electrons observed by the Arase satellite.

1 Introduction

Whistler mode chorus waves are bursty electromagnetic emissions that are often observed as the lower band mode below half of the electron cyclotron frequency f_{ce} and/or the upper band mode between $0.5f_{ce}$ and $1.0f_{ce}$. The Earth's magnetosphere naturally generates the whistler chorus with the injection of several tens of keV electrons associated with substorms (e.g., Tsurutani & Smith, 1977; Miyoshi et al., 2003, 2013). The whistler chorus waves play an important role in accelerating energetic electrons over a wide energy range on the keV to MeV order through Doppler-shifted cyclotron resonance (Horne & Thorne, 2003). Cyclotron resonant interactions result in the pitch angle and energy diffusion of electrons bouncing along a magnetic field line, and more energetic electrons can resonate with chorus waves at higher magnetic latitudes. A quasi-linear theory, which assumes the resonant interactions by incoherent, broadband, and small-amplitude whistler waves, is commonly used to describe the evolution of the phase space density of radiation belt electrons. Numerical simulations based on the theory reproduce the evolution of electrons trapped in the Earth's magnetosphere on a time scale range from an hour to a day (Thorne et al., 2013; Glauert et al., 2014; Tu et al., 2014).

However, some previous observations suggest the rapid acceleration of energetic electrons on a time scale much shorter than the prediction based on a quasi-linear theory (Fennell et al., 2014; Kurita et al., 2018). This indicates that some efficient acceleration processes not described in this theory are involved. Many theoretical and simulation studies have shown the importance of a nonlinear scattering process associated with the coherent and bursty nature of the whistler chorus waves (e.g., Omura et al., 2007; Bortnik et al., 2008; Lakhina et al., 2010; Saito et al., 2016). The contribution of the coherent nature of chorus waves, which is beyond the scope of the quasi-linear theory, plays an important role in the efficient acceleration of energetic electrons. In particular, relativistic turning acceleration (RTA) (Omura et al., 2007) requires the coherent nature of whistler waves in order to efficiently accelerate electrons. Lakhina et al. (2010) also discussed the importance of the coherent and bursty nature of whistler chorus waves. They estimated the rate of the pitch angle change of electrons using coherent subelements with durations of tens of milliseconds or longer. For typical parameters of whistler chorus elements, their study showed that the coherent chorus elements can realize a more rapid pitch angle scattering of energetic electrons than a continuum of incoherent chorus waves as assumed in the quasi-linear theory. Previous studies have thus revealed that quasi-

linear models may underestimate electron scattering in terms of pitch angle and energy by whistler chorus bursts.

As studied by Kurita et al. (2018), the Arase satellite (Miyoshi, Shinohara, et al., 2018) observed the rapid flux enhancement of electrons with energies above 20 keV associated with an intense upper-band whistler chorus burst. They found that the evolution of electron pitch angle distributions in multi-energy channels occurs within 30 s. By detailed data analysis of the cyclotron resonant condition between electrons and the chorus burst, they concluded that the evolution is a consequence of wave–particle interactions, which are faster than expected from a quasi-linear theory. Thus, it is of considerable interest to examine numerically how the electrons are accelerated rapidly through the wave–particle interactions on such a short time scale, using in situ observational data obtained by Arase.

In this paper, we demonstrate electron scattering by an upper-band whistler chorus burst with a duration of 32 s, using a test-particle simulation: Geospace Environment Modeling System for Integrated Studies - Radiation Belt with Wave-particle interaction (GEMSIS-RBW) (Saito et al., 2012) with observational data obtained by the Medium Energy Particle Experiment-electron analyzer (MEP-e; S. Kasahara et al. (2018)) and Onboard Frequency Analyzer (OFA; Matsuda et al. (2018)) in Plasma Wave Experiment (PWE; Y. Kasahara et al. (2018)) onboard Arase. In Sec. 2, we describe the observational data set applied to the test-particle simulation. In Sec. 3, we describe the simulation model and its initial conditions. In Sec. 4, we compare the temporal variations of electron flux distributions resulting from the simulation with the observational data. Our test-particle simulation demonstrates that the upper-band whistler chorus burst reproduces the Arase observations through the electron scattering by the nonlinear phase trapping. In Sec. 5, we discuss the scattering processes in the whistler chorus burst, some problems of our simulation, and potential future works. Finally, we conclude that the nonlinear scattering, which should not be described by quasi-linear diffusion processes, plays an important role in the deformation of electron flux distribution in a short duration, as observed by Arase.

2 Arase observation

A rapid deformation of electron flux distribution at tens of keV during a period between 19:20:13 UT and 19:20:46 UT on 8 April 2017 was reported by Kurita et al. (2018). Arase was located near the magnetic equator (magnetic latitude of 0.2° – 1.5°), at the magnetic local time of 4.3 – 4.5 h, and the radial distance of 5.5 Earth radii, corresponding to the McIlwain L (L_m) of about 5.4. Magnetic field data obtained by the Magnetic Field Experiment (MGF; Matsuoka, Teramoto, Nomura, et al. (2018)) onboard Arase show a background magnetic field intensity of 170 nT, indicating the local electron cyclotron frequency f_{ce} of 4.7 kHz. The plasma density $N = 3.4$ cm^{-3} was estimated by Kurita et al. (2018) on the basis of HFA and MGF measurements, where HFA is the high-frequency analyzer onboard Arase (Kumamoto et al., 2018), indicating the local electron plasma frequency f_{pe} of 16.5 kHz and thereby the frequency ratio f_{pe}/f_{ce} of about 3.5.

Figure 1 is the summary plot of the event. The OFA magnetic spectrum (top panel) shows an intense upper-band whistler chorus burst at frequencies over $0.5f_{ce}$. The wave amplitude is highly variable in time and frequency. The maximum instantaneous amplitude of the magnetic fluctuation exceeds 100 pT. Kurita et al. (2018) estimated the wave normal angle of the upper-band whistlers by the singular value decomposition method (Santolík et al., 2003). They found that the burst propagates in the quasi-parallel direction of the background magnetic field. Bottom panels of Figure 1 show electron flux distributions obtained by MEP-e at four time intervals. Over 32 s represented by the panels, the flux of >20 keV increases at pitch angles of 70 – 80 degrees, while the flux of <20 keV decreases at pitch angles of 40 – 50 degrees. Because the flux variation seems to occur on the resonant ellipses of the upper-band whistlers, Kurita et al. (2018) concluded that the low-energy electrons are accelerated to higher energies through the cyclotron resonance with the upper-band whistler chorus burst.

3 Simulation models and initial conditions

We perform a test-particle simulation that demonstrates the electron scattering by the upper-band whistler chorus burst on a magnetic field line. The upper-band whistlers are assumed to be generated at the magnetic equator and propagate away from the equator along the field line. We set wave amplitudes and frequencies on the basis of the OFA

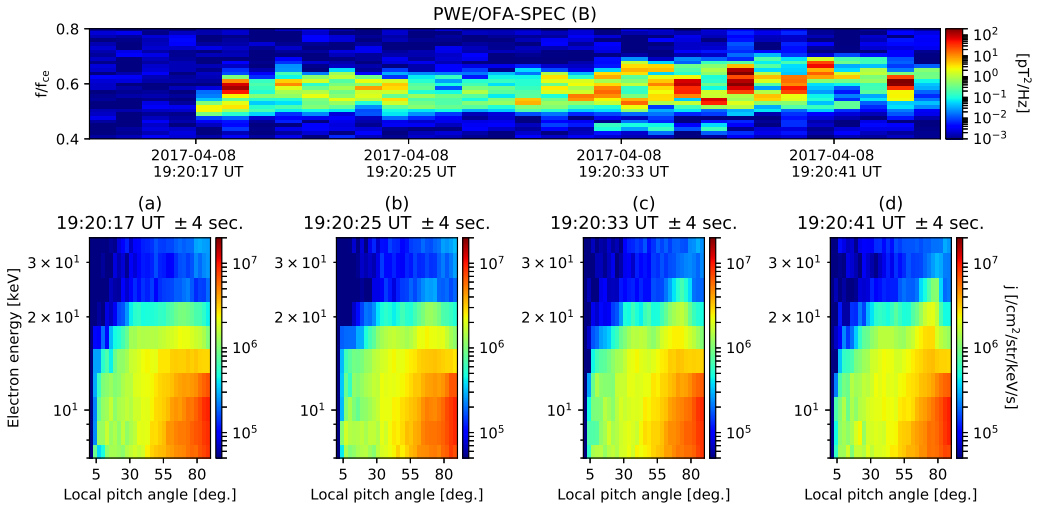

Figure 1. Observation by Arase located at the magnetic latitude of 0.2° - 1.5°, the magnetic local time of 4.3 – 4.5 h, and the radial distance of 5.5 Earth radii ($L_m \sim 5.4$). (Top) Dynamic frequency spectrum of magnetic fluctuations obtained from PWE/OFA. (Bottom) Electron flux distributions as functions of pitch angle and energy obtained from MEP-e at time intervals at around 19:20:17, 19:20:25, 19:20:33, and 19:20:41 UT. Electrons responsible for each flux distribution are detected in the time range of ± 4 s.

magnetic field spectrum shown in Fig. 1. The simulation solves the equations for adiabatic and non-adiabatic momentum change of 10^6 electrons by the upper-band whistlers. We set particle weights for all the electrons on the basis of the electron flux distribution obtained by MEP-e before the upper-band whistlers are enhanced. By using the weights for the electrons, we can calculate the time variation of the electron flux distribution at any place along the field line throughout the simulation. The following subsections describe the details of the test-particle model, the wave model, and the initial condition used in the simulation.

3.1 Test-particle model

We use the test-particle simulation code GEMSIS-RBW (RBW) (Saito et al., 2012) to demonstrate the temporal variation of energetic electron flux distribution. Using the RBW simulation model, we calculate the adiabatic motion of electrons along a field line

using the equations of magnetic mirror motion of the guiding center,

$$\frac{dp_{\parallel}}{dt} = -\frac{\mu}{\gamma}\frac{\partial B}{\partial s}, \tag{1}$$

$$\frac{ds}{dt} = \frac{p_{\parallel}}{m_o\gamma}, \tag{2}$$

where $\mu = p_{\perp}^2/(2m_oB)$ is the first adiabatic invariant. The invariant is assumed to be constant as the mirror force is solved with the equation. Here, the relativistic Lorentz gamma γ is $\sqrt{1+p^2/(m_oc)^2}$, B is the magnetic field intensity at the electron position s, $p^2 = p_{\parallel}^2 + p_{\perp}^2$, $p_{\parallel}$ and $p_{\perp}$ are electron momenta parallel and perpendicular to the magnetic field, respectively, m_o is electron rest mass, and c is the light speed. The equations are solved by using the 4th-order Runge–Kutta method. In addition to the adiabatic mirror motion, the RBW simulation demonstrates the propagation of wave packets along the field line with its own group velocity. The group velocity based on the cold plasma dispersion relation is calculated at packet positions. Each wave packet has a wave amplitude and frequency, which are constant over time.

By calculating multiple packets traveling along the field line in the RBW model, we can estimate the wave frequency and amplitude acting on each of the electrons on the field line. The wavenumber at the electron position k_s is calculated from the linear dispersion relation of whistler waves with the the frequency f_s, and then right circularly polarized electromagnetic fluctuations $\delta\mathbf{E}$ and $\delta\mathbf{B}$ at the electron position are constructed using the RBW model. The temporal variation of the magnetic wave phase ϕ at the electron position is

$$\phi = 2\pi f_s t - k_s v_{\parallel} t + \phi_o. \tag{3}$$

Here, ϕ_o is the wave phase at which the wave-particle interaction starts. Note that ϕ is assigned to each of the electrons, which is the important core method for the RBW model. By using the electromagnetic fluctuations, we can solve the following equation of motion using the RBW model,

$$\frac{d\mathbf{p}}{dt} = q_e\left(\delta\mathbf{E} + \mathbf{v}\times(\mathbf{B}+\delta\mathbf{B})\right), \tag{4}$$

where $\mathbf{v}$ is the vector of electron velocity. Wave data applied to Eq. (4) are updated every Δt (~ 0.035 ms) which is the time resolution of the solver of the guiding-center equations (Eqs. (1) and (2)), whereas the time resolution for the equation of motion (Eq. 4) is $\delta t = \tau_{gyro}/64$, which is quite shorter than Δt, where τ_{gyro} is the in situ electron gyration period. The equation of motion is solved by the Buneman–Boris method (Buneman,

1993). The equation of motion is used to calculate $\Delta\mathbf{p}$, which is the change in $\mathbf{p}$ in Δt; then $\Delta\mathbf{p}$ is reflected in the guiding-center equations (Eqs. (1) and (2)). Then, the first adiabatic invariant μ is updated using the magnetic field intensity at the electron position, corresponding to the break of μ caused by the electron scattering. By using the above sequence of calculations, we can solve the equations of magnetic mirror motion coupled with the equation of motion in electromagnetic fluctuations of whistler mode waves propagating along the field line. The RBW model has been successfully applied to various wave-particle interaction phenomena in radiation belts, pulsating auroras, and microbursts (Saito et al., 2012, 2016; Miyoshi, Oyama, et al., 2015; Miyoshi, Saito, et al., 2015; Miyoshi et al., 2020).

3.2 Wave model

Wave packets are released every 1 ms from the magnetic equator according to the OFA magnetic spectrum shown in Fig. 1. The OFA resolves 15 frequencies between $0.5f_{ce}$ and $0.7f_{ce}$. The frequency of each wave mode is defined as the discrete frequency f^i,

$$f^i = f_o + \Delta f \times i, \tag{5}$$

where f_o is 2.368 kHz, Δf is 64 Hz, and i is an integer between 1 and 15. Since the time resolution of the OFA is 1 s, the amplitude of wave packets released every Δt varies every second. When there are multiple modes at the electron position, the RBW model is used to construct electromagnetic fluctuations acting on the electron by linearly superimposing these modes. On the basis of statistical studies of the upper band chorus distribution (e.g., Bortnik et al., 2007), we assume that wave packet propagation is limited to a magnetic latitude of 10 degrees. Note that there is no correlation of wave phase among wave modes in the simulation. Moreover, we assume that the phase difference between the wave phase and the electron gyrophase is randomly set between 0 and 2π when the electron passes through the magnetic latitudes of 10 degrees from higher latitudes.

3.3 Initial conditions

The magnetic field intensity along the field line in this simulation is assumed to be equal to the Earth's dipole field. On the basis of the MGF data of Arase, which was located close to the magnetic equator, the equatorial magnetic field intensity B_{eq} is estimated to be 170 nT. The background magnetic field is assumed to be the dipole field;

thus, the magnetic field strength along the field line is

$$B(\lambda) = 170 \times 10^{-9} \frac{\sqrt{1 + 3\sin^2 \lambda}}{\cos^6 \lambda}, \tag{6}$$

where λ is latitude. On the basis of the HFA and MGF measurements, as described in Sec. 2, the estimated plasma density $N = 3.4$ cm^{-3} is applied in this simulation. Here, as in the previous simulation (Miyoshi, Oyama, et al., 2015), we assume that the plasma density is constant along the field line up to the magnetic latitude of 10 degrees.

The number of electrons in the present simulation is 10^6. These are distributed along the magnetic field line with random bounce phases. Their equatorial pitch angles range from the loss cone angle to slightly less than 90 degrees, and the kinetic energy ranges from 5 to 40 keV. The weight of electrons at energy E and the equatorial pitch angle α_{eq} are derived from the weight table W,

$$W(E, \alpha_{eq}) = \frac{j(E, \alpha_{eq})}{j_u(E, \alpha_{eq})}. \tag{7}$$

Here, $j(E, \alpha_{eq})$ is the flux distribution to be reproduced, and $j_u(E, \alpha_{eq})$ is the flux distribution calculated from the electrons with the unit weight. $j(E, \alpha_{eq})$ can be reproduced by setting the weight of the electrons. The weight of electrons is determined to fit the distribution function obtained by MEP-e just before the chorus burst appears. The weight is constant over time and there is no additional injection of electrons throughout the simulation. The simulation starts from 2017-04-08 19:20:13 UT at which wave packets start to inject from the equator following the OFA shown in Figure 1. The simulation time t is the time that elapsed from the start.

4 Simulation results

Figure 2 shows electron flux distributions calculated at the equator in the simulation. The time intervals labeled on the panels (a – d) correspond to the time intervals of observations for the flux distributions shown in the lower panels in Figure 1. The temporal evolution of electron fluxes shows that the electron flux increases at energies higher than 20 keV within 32 s. At energies lower than 20 keV, the electron flux at the pitch angles of 40 – 50 degrees decreases. These characteristics of flux deformation are similar to those of MEP-e shown in Figure 1.

To compare these distributions more directly, we plot the pitch angle distributions at 14.3, 17.1, 20.5, and 24.5 keV of the Arase observations (blue lines) with those of the

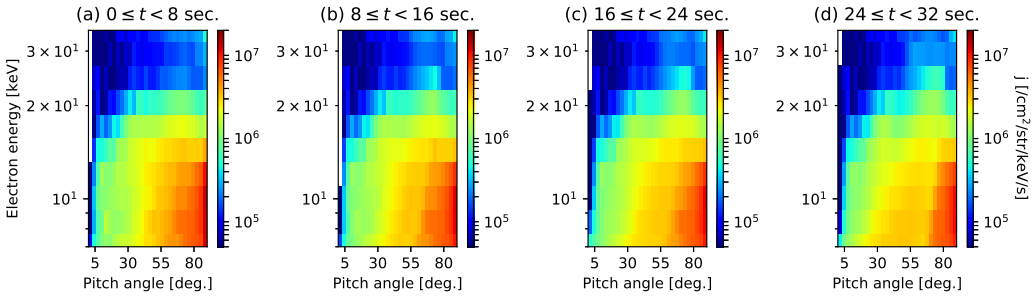

Figure 2. Equatorial electron flux distributions calculated from RBW simulation as a function of pitch angle and energy. The flux distributions are calculated during (a) $0 \leq t < 8$ s, (b) $8 \leq t < 16$ s, (c) $16 \leq t < 24$ s, and (d) $24 \leq t < 32$ s. These time ranges correspond to 19:20:17 UT ± 4 s, 19:20:25 UT ± 4 s, 19:20:33 UT ± 4 s, and 19:20:41 UT ± 4 s, respectively.

simulation (red lines) in Figure 3. The Arase observations over 8 s are averaged, whereas black error bars show the standard deviations of the Arase observations at each pitch angle and energy bins during the indicated time interval. In both the simulation and observation, electron fluxes at around the pitch angle of 50 degrees decrease over time at energies of 14.3 and 17.1 keV, whereas those at around the pitch angle of 75 degrees at energies of 20.5 and 24.5 keV increase. A butterfly distribution is formed at energies higher than 20 keV. It is shown that the simulation reproduces the characteristics of the observed flux enhancement.

Figure 4 shows the initial flux distributions of electrons that contribute to the fluxes within the energy range between 23.5 and 25.5 keV and the pitch angle range between 70 and 80 degrees in (a) $0 \leq t < 8$, (b) $8 \leq t < 16$, (c) $16 \leq t < 24$, and (d) $24 \leq t < 32$ s. Here, we define the pitch angle and energy ranges as Λ. As shown in panel (a), the initial flux distribution of electrons has a peak in the Λ at the time of less than 8 s. Only a small fraction of the electrons originate from outside of Λ at this moment. At later times, as shown in panels (b-d), the distribution spreads in both directions of energy and pitch angle, and the peak of the flux distribution moves toward lower energies and smaller pitch angles. At the time interval shown in panel (d), there is a peak of the distribution at the pitch angle between 40 and 50 degrees and the energy between 15 and 16 keV, indicating that the electrons that were initially distributed there dominate Λ.

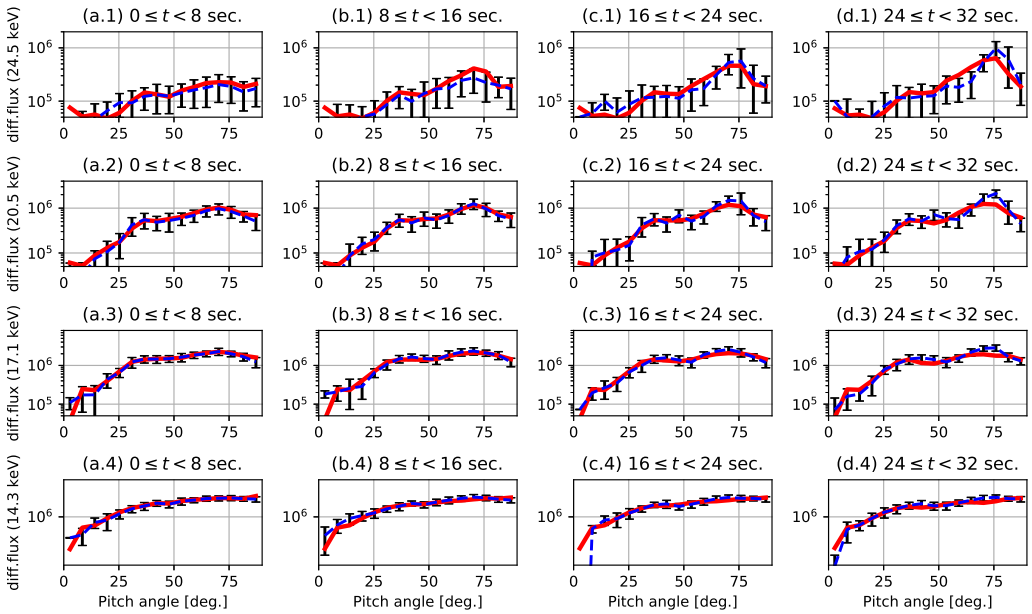

Figure 3. Pitch angle distributions at 14.3, 17.1, 20.5, and 24.5 keV. Blue lines are electron fluxes taken from the MEP-e onboard Arase averaged over 8 s, black error bars are the standard deviations of the fluxes obtained during the time interval, and red lines are calculated from the RBW simulation.

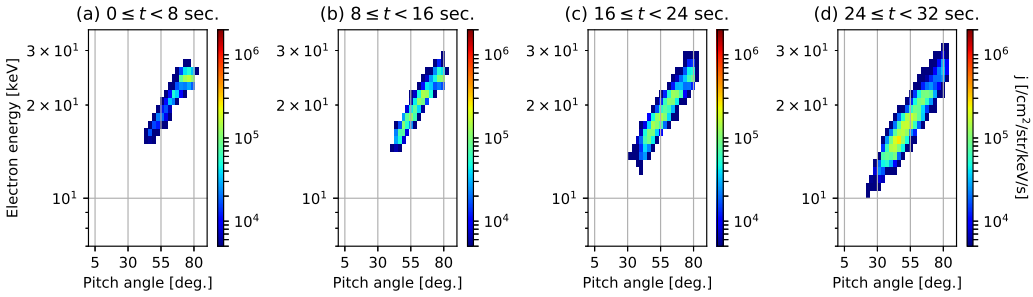

Figure 4. Initial flux distributions of electrons contributing to flux within the energy range between 23.5 keV and 25.5 keV and the pitch angle range between 70 and 80 degrees in the time ranges of (a) $0 \leq t < 8$, (b) $8 \leq t < 16$, (c) $16 \leq t < 24$, and (d) $24 \leq t < 32$ s.

Figure 5 confirms whether the pitch angle change can be realized with a quasi-linear diffusion model. The black-dashed line in the top panel shows the magnetic wave power in frequency averaged in time during the burst event, calculated from the OFA magnetic spectrum. The dashed red line is a Gaussian fitting curve for the time-averaged frequency spectrum. The Gaussian fitting gives the maximum amplitude of 33.6 pT, the center of frequency of $0.59 f_{ce}$, and the frequency band width of $0.027 f_{ce}$. With the derived parameters of the magnetic wave power distribution, we calculate the pitch angle diffusion coefficients of the quasi-linear diffusion model (Albert, 1999) at energies of 10, 20, and 30 keV. Here, the coefficients are averaged in the bounce motion. As electrons move along the distribution shown in Figure 4(d) before reaching Λ, the averaged pitch angle coefficient of the electrons would be less than $2{\times}10^{-3}$ [/sec.]. We found in Figure 4 (d) that the main flux source contributing to the formation of the butterfly distribution is at a pitch angle between 40 and 50 degrees and an energy between 15 and 16 keV. From a simple estimation, a value corresponding to a pitch angle diffusion coefficient is about 4×10^{-3} [/sec.] as electrons at the source region ($\alpha_{eq} = 45$ degrees) move to the flux peak at 24.5 keV ($\alpha_{eq} = 75$ degrees) within 32 s. This value seems to be slightly larger than the diffusion coefficients estimated using the quasi-linear diffusion model, but roughly of the same order. It suggests that some electrons initially at 15 keV can contribute to the butterfly distribution formation through pitch angle scattering with comparable timescales predicted by the quasi-linear process.

Figure 6 shows the probability of nonlinear scattering of electrons with energies between 24 and 25 keV at t = 32 s as a function of equatorial pitch angle. The probability is defined as N_{rapid}/N_{total} with the energy range in a pitch angle bin, where N_{rapid} is the number of electrons that have experienced a rapid change in the pitch angle and the energy at least once during 32 s and N_{total} is the total number of electrons. Here, the number of electrons in each bin is calculated considering particle weights defined by the initial flux distribution. The rapid change for an electron means that a value of $D_{TP} = \Delta\alpha_{eq}^2/(2\Delta t)$ corresponding to an instantaneous pitch angle diffusion coefficient exceeds the threshold coefficients D_{th} = 0.05, 0.1, and 0.2, where $\Delta\alpha_{eq}$ is an equatorial pitch angle change calculated every $\Delta t = 0.2$ s. The threshold coefficients are 20 - 100 times larger than the pitch angle coefficients in Figure 5. As seen in Figure 6, there is a peak in pitch angles of 70 and 80 degrees at each D_{th}. Around a pitch angle of 75 degrees, almost all electrons experience $D_{TP} > 0.05$ at least once during the burst. The value is

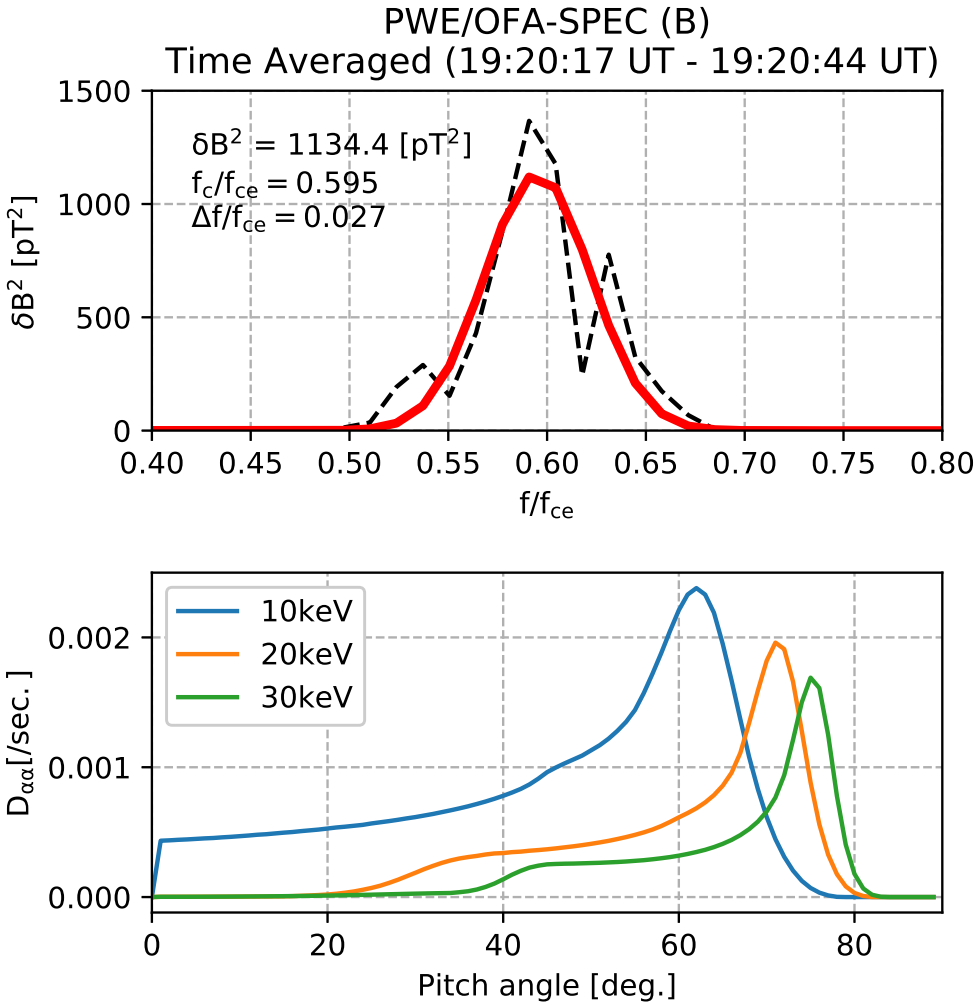

Figure 5. (Top) Magnetic frequency spectrum averaged in time during the burst event obtained from PWE/OFA (Black-dashed) and a Gaussian fitting curve for the time-averaged frequency spectrum (Red). (Bottom) Bounce-averaged, pitch angle diffusion coefficients as a function of pitch angle with energies of 10, 20, and 30 keV. The quasi-linear model uses the Gaussian distribution of magnetic wave power as shown in the top panel, which has the maximum amplitude of 33.6 pT, the center of frequency of $0.59 f_{ce}$, and the frequency band width of $0.027 f_{ce}$. We assume a Gaussian distribution of the wave propagation angle with the half width of 45 degrees, centered at the zero degree along the magnetic field line.

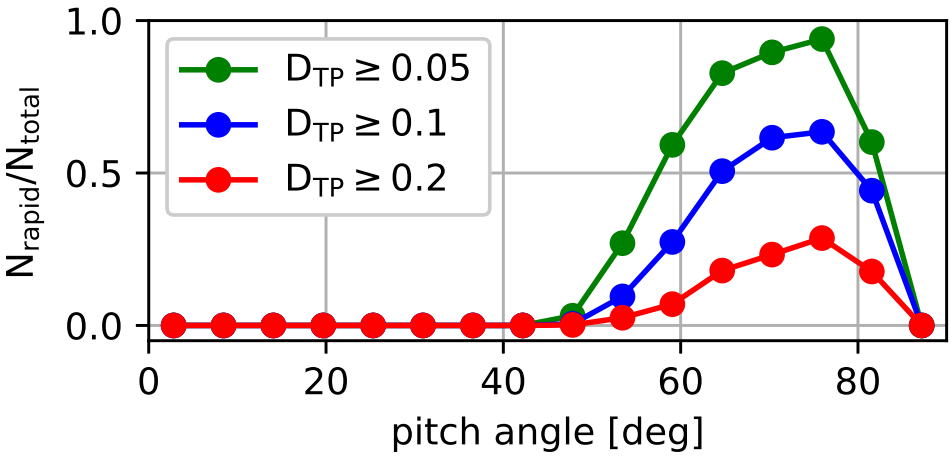

Figure 6. Probability of nonlinear scattering for electrons with energies between 24 and 25 keV at t = 32 s as a function of equatorial pitch angle.

about 20 times larger than the diffusion coefficients. About 30% of electrons at the peak experience a rapid scattering with $D_{TP} > 0.2$, which is 100 times larger than the estimation with the quasi-linear model. The peaks of N_{rapid}/N_{total} in pitch angle are within a range of electron flux enhancement shown in the top panels (E = 24.5 keV) in Figure 3. From the OFA spectrum (Figure 1), the maximum instantaneous amplitude is estimated to be about 120 pT, which is four times higher than the average amplitude. If we assume a 16 (= 4^2) times higher magnetic power distribution, pitch angle diffusion coefficients would be estimated to be up to 0.032 [/sec.]. The diffusion coefficients estimated using the quasi-linear model cannot exceed 0.05.

We examine linear/nonlinear scattering processes in more detail by analyzing the motion of typical electrons in the simulation. Figure 7 shows the time histories of energy and equatorial pitch angle of five electrons labeled as A to E, which are sampled from 100 electrons with energies between 15 and 16 keV and equatorial pitch angles between 40 and 50 degrees at t=0. Because the whistlers propagate away from the equator up to the magnetic latitude of 10 degrees, electrons have opportunities to be scattered through cyclotron resonance when they travel toward the equator at magnetic latitudes less than 10 degrees. Thus, electrons can be scattered every half of the bounce period ($\sim$ 0.5 s), as seen in all the time histories. Almost all scattering times are on the order of 100 ms or shorter. In many cases, electrons experience energy changes of less

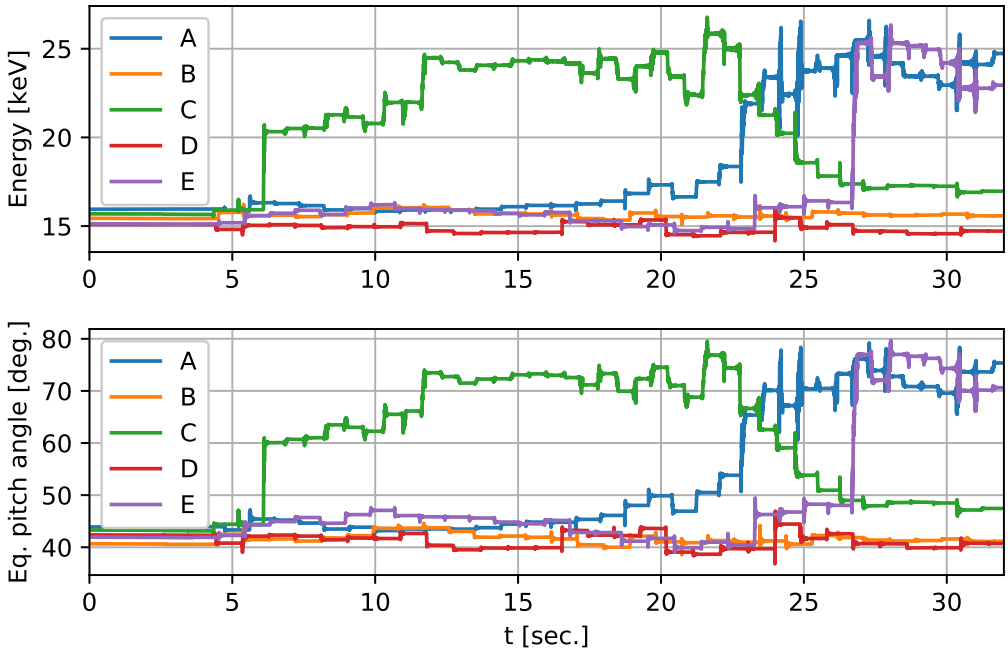

Figure 7. Time histories of the energy (top) and equatorial pitch angle (bottom) of five electrons labeled as A to E. The initial pitch angle and energy are between 40 and 50 degrees and between 15 and 16 keV, respectively.

than 1 keV, but in some cases, the interaction increases or decreases their energy higher than 1 keV at a single scattering.

Figure 8 shows the results of a detailed analysis of electron E. The top panel shows the energy time history of electron E, which is the same as that shown as the purple line in Figure 7. For the simulation time of less than 26 s, the electron undergoes energy changes of 1 keV or less in each of the scattering events. We label one of the events as (I). In the time range between 26 and 27 s, the electron gains an energy of about 8 keV, which is labeled as (II). Soon after the efficient energy gain, the electron loses an energy of about 2 keV, which is labeled as (III). For the three events labeled here, we show the distance of the electron from the magnetic equator (2nd row), the kinetic energy (3rd row), the inhomogeneity ratio S (4th row), and the phase differences ζ between the wave phase and the electron gyrophase (5th row). As described by Omura et al. (2007), the inhomogeneity ratio is

$$S = \frac{1}{2kv_\perp \Omega_w \delta^2} \left[\left(2 + \delta^2 \frac{\Omega_e - \gamma\omega}{\Omega_e - \omega} \right) V_R - \frac{k\gamma v_\perp^2}{\Omega_e} \right] \frac{\partial \Omega_e}{\partial s}, \tag{8}$$

where $\delta^2 = 1 - (\omega/ck)^2$, $\Omega_w = -q_e \delta B/m_o$, $V_R = (\omega - \Omega_e/\gamma)/k$, $v_\perp$ is the speed of an electron in the direction perpendicular to the background magnetic field, and Ω_e is the angular electron cyclotron frequency. The inhomogeneity ratio and the phase difference are calculated for 15 wave modes described in Sec. 3.2.

To estimate the energy change and the interaction time of each of the events, we calculate the fitting curve using the function based on the hyperbolic tangent curve,

$$F(t) = \frac{\Delta E}{2}\left(1 + \tanh\frac{t - t_c}{t_w}\right) + E_o, \tag{9}$$

by solving a nonlinear least-squares problem by an algorithm (Branch et al., 1999) that is used in the function `scipy.optimize.curve_fit()` in SciPy library (Virtanen et al., 2020). Here, ΔE is the amount of energy change, t_c is the center time of the scattering event, t_w is the half width of the time interval of the energy change, and E_o is the initial value of the function. The curve obtained using the estimated parameters is shown as the blue dashed lines in the third row in Figure 8, and the parameters are shown in each of the panels. Event (I) has the smallest energy change (ΔE =130 eV) with the shortest duration of 4.8 ms ($= 2t_w$) among the three events. On the other hand, event (II) has the longest duration of 100.4 ms with the largest energy change (7.98 keV). Event (III) shows the energy reduction (-1.93 keV) with a moderate duration of 27.4 ms. Note that the pitch angle immediately before the rapid energy loss is relatively large ($\alpha_{eq} >$ 75 degrees), as is shown in Figure 7.

We calculate the inhomogeneity ratio S (Omura et al., 2007) for 15 wave modes, which is the key parameter for the resonant phase trapping of electrons. The necessary condition for the trapping is $|S| \leq 1$, which satisfies the pendulum equation for the phase difference ζ. When the pendulum equation is satisfied, the electrons are trapped in the wave phase and then gain energy efficiently. Bortnik et al. (2008) defined the inhomogeneity forcing term ρ, which is used to categorize three scattering types: the linear scattering, the phase trapping, and the phase dislocation. The condition of $\rho < 1$ leads to the diffusive behavior of electrons, whereas the condition of $\rho \gg 1$ leads to the phase dislocation, which generally reduces the electron energy. When $\rho \sim 1$, some electrons are trapped by a wave, leading to the efficient energy gain of electrons. Saito et al. (2016) showed that $S^2\rho^2 = 1$, so the three types of scattering are also categorized on the basis of S, namely, $|S| \gg 1$ for linear scattering, $|S| \sim 1$ or slightly less for the phase trapping, and $|S| \ll 1$ for the phase dislocation. The inhomogeneity ratio for 15 wave

modes in event (I) shows that all $|S|$ values are much larger than 1 within the duration of the small energy change, indicating the linear scattering. The time histories of ζ for 15 wave modes do not show any signature of the phase trapping. Several high-frequency modes have ζ decreasing monotonically, whereas others have convex profiles indicating that the resonance conditions $d\zeta/dt \sim 0$ are satisfied at the peak of ζ. In event (II), several wave modes have $|S| \sim 1$ or slightly less during the efficient energy gain. The phase differences ζ of several modes remain roughly constant. It means that the electron is phase-trapped by some of these modes. Thus, the electron undergoes efficient energy gain over a duration longer than that of event (I). In the case of event (III), several wave modes have S values close to zero, and the electron loses energy, whereas $d\zeta/dt$ of the wave modes is close to zero. The signature of event (III) is consistent with that of the phase dislocation.

We calculate the energy time histories of 100 electrons that have had the initial energy between 15 and 16 keV and the initial equatorial pitch angle between 40 and 50 degrees. From the entire dataset of the time histories, we estimate t_c and ΔE in each of the scattering events by using the fitting method as used in Figure 8. In each of the scattering events, we calculate the inhomogeneity ratio for 15 wave modes at t_c. A total of 3,413 scattering events are identified from the dataset. Here, we choose scattering events whose standard deviation of ΔE is smaller than the estimated ΔE. The qualified event list is further grouped into two classes: weak and intense, according to the magnitude of ΔE, which are defined as $10\text{eV} \leq |\Delta E| < 100\text{eV}$ and $1\text{keV} \leq |\Delta E| < 10\text{keV}$, respectively. We further classify each of the two classes of the events into two types according to the sign of ΔE, that is, positive and negative.

Figure 9 shows the probability density functions (PDFs) of the inhomogeneity ratio S calculated at t_c for the two types in two classes. Note that the integral of the PDFs over S becomes unity. The number of identified events for each of the four cases is shown as N. The PDFs for intense events (left panels) show a clear peak at $|S|$ slightly lower than 1. According to the classification of the scattering processes discussed by Bortnik et al. (2008), the intense events are expected to be accompanied by phase trapping or phase dislocation. Considering the characteristics of the scattering processes, it is shown that the phase trapping and phase dislocation contribute to the intense-positive and intense-negative events, respectively. Note that the PDFs of the intense-negative events show the distribution confined slightly closer to $|S| = 0$ than that of the intense-positive events.

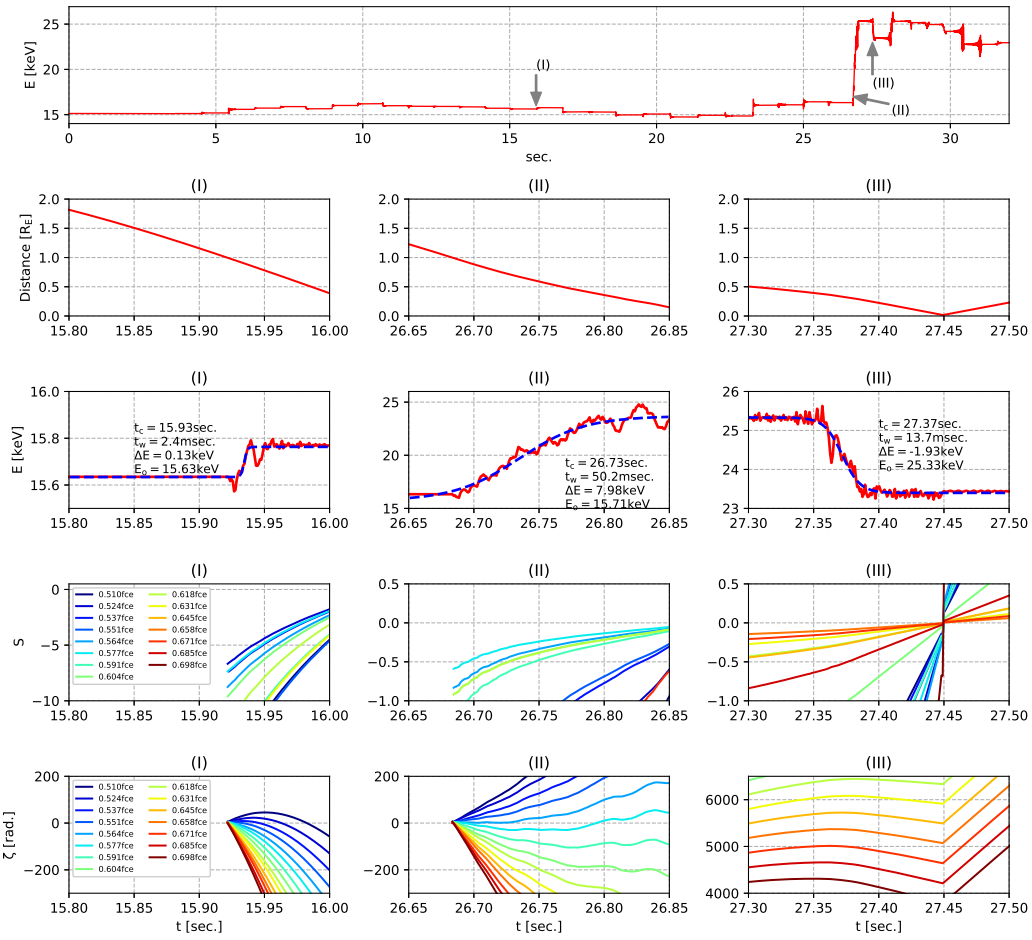

Figure 8. Results of a detailed analysis of electron E. (Top panel) Time history of the electron energy. (2nd row) Distance from magnetic equator in events (I), (II), and (III) labeled in top panel. (3rd row) The red line shows an enlarged view of the time history of the electron energy in each of the events. The blue dashed line is the curve fitting of the red line through the hyperbolic tangent function. The fitting parameters are shown in each of the panels. (4th row) Inhomogeneity ratio of the electron E associated with 15 wave modes. (Bottom row) Phase differences between the electron gyrophase and the wave phases of 15 wave modes.

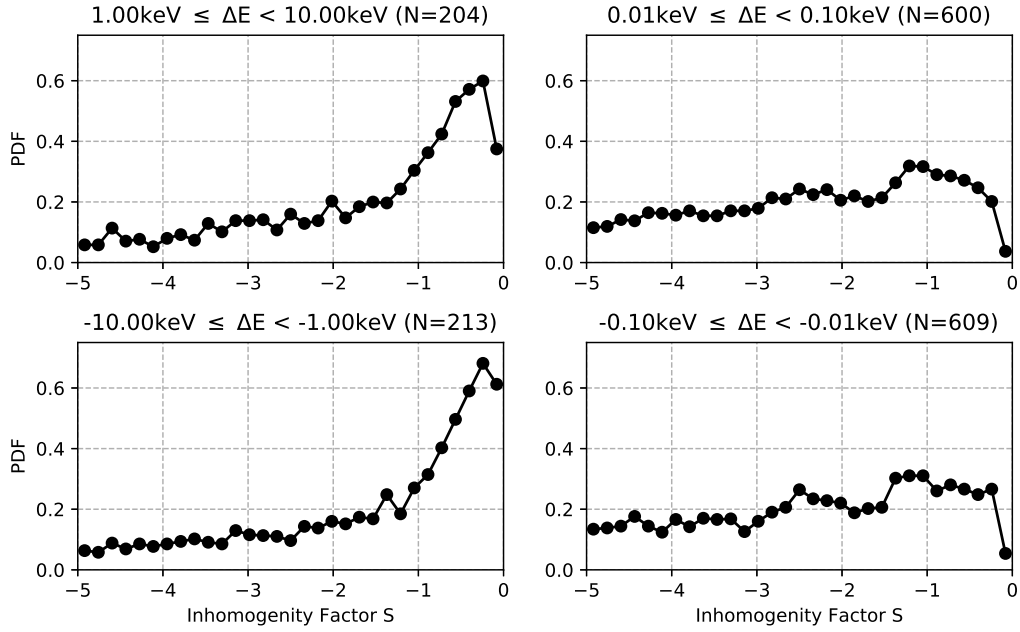

Figure 9. Probability distribution functions of the inhomogeneity ratio S for (upper left) intense-positive, (lower left) intense-negative, (upper right) weak-positive, and (lower right) weak-negative scattering events. The scattering events are identified from the energy–time histories of 100 electrons by the fitting method of the hyperbolic tangent fitting function for estimating t_c and ΔE. The inhomogeneity ratios for 15 wave modes for each of the electrons are calculated at t_c.

The slight difference in the distributions may reflect the differences in the conditions between the phase dislocation and the phase trapping. In weak events, there is no significant peak on the PDFs. Moreover, unlike the intense events, the PDFs tend to become smaller with decreasing $|S|$ when $|S| < 1$. On the other hand, at $|S| > 1$, the PDFs tend to be higher and relatively flatter than those in intense events. It is indicated that the linear scattering, which has $|S| \gg 1$, dominates both the weak-positive and weak-negative events.

Table 1 shows the probabilities calculated from the integral of PDFs in $|S| < 1$ for the four categorized events. The integral of the PDF for the intense-positive events shows that roughly half of the wave modes at t_c have $|S| < 1$. The intense-negative events also show the high probabilities of wave modes with $|S| < 1$. It is clear that the wave modes that lead to nonlinear scatterings definitely contribute to the intense events. On

Table 1. Integral of PDFs in $|S| < 1$ for each of the scattering events.

	Intense	Weak
Positive	46.1 %	21.4 %
Negative	49.9 %	22.1 %

the other hand, in weak events, about 80% of the wave modes are found to be beyond the range ($|S| > 1$), indicating the dominance of the linear scattering.

5 Discussion

Our simulation results reproduce the temporal variation of the electron flux distribution observed by Arase (Figures 1-3). A pitch angle distribution at 24.5 keV produces a butterfly distribution within 32 s because of an upper-band chorus burst. It has a flux peak of the pitch angle between 70 and 80 degrees. The main flux source contributing to the formation of the butterfly distribution is at a pitch angle between 40 and 50 degrees and an energy between 15 and 16 keV at t=0 (Figure 4). From a simple estimation, we confirmed that some electrons initially at 15.5 keV may possibly contribute to the formation of the butterfly distribution through a quasi-linear process (Figure 5). However, we found that the instantaneous pitch angle changes (D_{TP}) of some electrons are much larger than those in the quasi-linear process. Electrons that experience $D_{TP} \geq 0.1$ within 32 s are dominant in the peak of the butterfly distribution (Figure 6). It suggests the importance of individual scattering processes not exactly described in quasi-linear processes. Furthermore, a timescale (Δt) for a pitch angle change of an electron is different in each scattering and tends to be shorter than 200 ms (See timescales of t_w shown in Figure 8). Thus, the instantaneous pitch angle changes (D_{TP}) with $\Delta t = 200$ ms tend to be underestimated here. We suggest that the contribution of the rapid scattering processes to the butterfly distribution is more important than our estimations. Lakhina et al. (2010) reported that instantaneously coherent chorus waves can realize a more rapid pitch angle scattering of electrons than that expected in quasi-linear models. The OFA spectrum (Figure 1) frequently shows relatively narrow frequency spectra, so the scattering process proposed by Lakhina et al. (2010) could work effectively. Moreover, when a wave amplitude of a narrow frequency spectra exceeds a certain threshold, phase trap-

ping/dislocation largely increases/decreases the pitch angle and energy of electrons, as shown in Figures 7 and 8. The pitch angle and energy transports by the phase trapping/dislocation show large D_{TP} of electrons, which contribute to the formation of the butterfly distribution. Recently, Gan, Li, Ma, Artemyev, and Albert (2020) have also reported the importance of nonlinear scattering in rapid electron acceleration at energies of tens of keV in terms of the formation of a butterfly distribution due to whistler chorus bursts. The scattering in instantaneously coherent chorus waves and the scattering by phase trapping/dislocation are not described as quasi-linear models. We expect that non-quasi-linear processes play an important role in forming a butterfly distribution of energetic electrons. Furthermore, the phase trapping process plays a more important role than the dislocation process, because the phase dislocation reduces the energy of electrons. The phase trapping would have a dominant contribution to the rapid acceleration of electrons that form the butterfly distribution at 24.5 keV.

In our simulation, there is no phase correlation among the wave modes, as described in Sec. 3.2. Usually, electrons are not easily trapped by broadband fluctuations with random wave phases. However, if there is an amplitude modulation in time and frequency, a particular wave mode can possibly be dominant. As a situation in which the wave mode that has $|S| \sim 1$ continues for a finite time, efficient acceleration associated with the phase trapping can occur even if there is no phase coherency with other wave modes with lower amplitudes.

The upper-band chorus burst used in the simulation is highly modulated in amplitude (Figure 1). The wave amplitude in the burst intermittently exceeds 100 pT in a narrow frequency range of about 100 - 200 Hz. Thus, some electrons are phase-trapped and gain energy in a short duration owing to intermittently enhanced wave modes (Figure 8). It is expected that the energy gain by the phase trapping is more efficient than the quasi-linear diffusion process even without a long-duration trapping ($\sim$ 1 sec.), as described by Omura et al. (2007). Recently, the important role of the phase trapping process in an amplitude-modulated whistler chorus wave has also been studied numerically by Hiraga and Omura (2020) and Gan, Li, Ma, Albert, et al. (2020). Our simulation and other numerical studies suggest the importance of considering realistic wave modes that contribute to electron accelerations. In quasi-linear diffusion models, statistical wave models are utilized, which eliminate the contribution of the amplitude modulation by averaging in time. The model that takes averaged signatures of waves may underestimate

the acceleration of electrons by each of the whistler chorus bursts or elements. In theoretical and numerical studies, appropriate wave models should be chosen to reproduce transient energetic electron dynamics that are actually observed in the magnetosphere.

As seen in Figures 7 and 8, the electron scattering shows not only small energy changes but also large energy changes induced by phase trapping and dislocation. A scattering process can be evaluated using an instantaneous inhomogeneity ratio S defined in Equation (8). The contribution of wave modes with $|S| \gg 1$ to electrons becomes dominant when the energy change is small, whereas that with $|S| < 1$ becomes dominant when the energy change is large (Figure 9). Larger wave amplitudes reduce $|S|$ because of the Ω_w^{-1} term, and the electron position also contributes to the reduction in $|S|$ because $|\partial\Omega_e/\partial s|$ tends to be smaller at lower latitudes. Note that $\partial\Omega_e/\partial s$ at the electron position is proportional to the spatial gradient of the background magnetic field along its field line. An instantaneous change of an inhomogeneity factor leads to a variety of scattering processes for an electron in the upper-band chorus burst.

The wave model used in the RBW simulation shown in this paper has a frequency gap of 64 Hz among wave modes, and thus, it does not perfectly construct the incoherent wave burst as defined in a quasi-linear diffusion model. Moreover, the time resolution of the wave model is limited to 1 s; thus, amplitude modulations shorter than 1 s are not reproduced. However, the simulation has demonstrated the Arase observations relatively well, implying that the observed upper-band whistler chorus burst may be close to the condition assumed in the wave model. That is, the observed burst might be coherent with a finite frequency (of about 64 Hz) and the amplitude modulation might not be much shorter than 1 s. It is necessary to consider the actual wave form data of whistler chorus waves covering a longer time scale in order to reproduce the actual electron scattering processes in future simulations.

6 Summary and conclusions

We have performed a data-driven RBW simulation using Arase observations to study the rapid flux enhancement of energetic electrons with the upper-band whistler chorus burst in the duration of about 30 s. The simulation reproduces the temporal variation of the electron flux distribution observed by Arase. As a result of detailed analysis of the simulation data, it is found that 15 – 16 keV electrons with the equatorial pitch an-

gle of 40 – 50 degrees contribute to the flux enhancement at energies higher than 20 keV at large pitch angles. We have found that scattering processes not described by the quasi-linear diffusion model contribute to the electron acceleration that forms the butterfly distribution at 24.5 keV. Our simulation suggests that a time-averaged statistical wave model as used in quasi-linear models underestimates the acceleration efficiency of radiation belt electrons in each of the whistler chorus bursts and elements.

We conclude that the rapid flux enhancement of energetic electrons observed by Arase is caused by the phase trapping of electrons associated with a highly amplitude-modulated upper-band whistler chorus burst. It is also suggested that the contribution of the amplitude modulation, which leads to the intermittent enhancement of the wave amplitude, should be properly taken into account in wave models for theoretical and numerical studies.

Acknowledgments

This work was supported by JSPS KAKENHI Grant Numbers JP15H05815 and JP20H01959. Science data of the ERG (Arase) satellite were obtained from the ERG Science Center (ERG-SC) operated by ISAS/JAXA and ISEE/Nagoya University (https://ergsc.isee.nagoya-u.ac.jp/index.shtml.en, Miyoshi, Hori, et al. (2018)). Part of the work of SK, YM, TH, MS, SN, and SI was carried out at ERG-SC. In this study, we analyzed the MEP-e level 3 v1.01, MGF level 2 v1.02 and the PWE/OFA-SPEC level 2 v2.01. Arase MGF Level-2 dataset used for this research is available in Matsuoka, Teramoto, Imajo, et al. (2018).

References

Albert, J. M. (1999). Analysis of quasi-linear diffusion coefficients. *Journal of Geophysical Research: Space Physics*, *104*(A2), 2429–2441. doi: 10.1029/1998JA900113

Bortnik, J., Thorne, R. M., & Inan, U. S. (2008). Nonlinear interaction of energetic electrons with large amplitude chorus. *Geophysical Research Letters*, *35*, L21102,. doi: 10.1029/2008GL035500

Bortnik, J., Thorne, R. M., & Meredith, N. P. (2007). Modeling the propagation characteristics of chorus using CRRES suprathermal electron fluxes. *Journal of Geophysical Research: Space Physics*, *112*, A08204. doi: 10.1029/2006JA012237

Branch, M. A., Coleman, T. F., & Li, Y. (1999). A Subspace, Interior, and Conjugate Gradient Method for Large-Scale Bound-Constrained Minimization Problems. *SIAM Journal on Scientific Computing*, *21*(1), 1–23. doi: 10.1137/S1064827595289108

Buneman, O. (1993). *Computer space plasma physics: Simulation techniques and software* (H. Matsumoto & Y. Omura, Eds.). Terra Scientific Publishing Company (TERRAPUB). Retrieved from `https://www.terrapub.co.jp/e-library/cspp/pdf/03.pdf`

Fennell, J. F., Roeder, J. L., Kurth, W. S., Henderson, M. G., Larsen, B. A., Hospodarsky, G., ... Reeves, G. D. (2014). Van Allen Probes observations of direct wave-particle interactions. *Geophysical Research Letters*, *41*, 1869–1875. doi: 10.1002/2013GL059165

Gan, L., Li, W., Ma, Q., Albert, J. M., Artemyev, A. V., & Bortnik, J. (2020). Nonlinear Interactions Between Radiation Belt Electrons and Chorus Waves: Dependence on Wave Amplitude Modulation. *Geophysical Research Letters*, *47*, e2019GL085987. doi: 10.1029/2019GL085987

Gan, L., Li, W., Ma, Q., Artemyev, A. V., & Albert, J. M. (2020). Unraveling the Formation Mechanism for the Bursts of Electron Butterfly Distributions: Test Particle and Quasilinear Simulations. *Geophysical Research Letters*, *47*, e2020GL090749. doi: 10.1029/2020GL090749

Glauert, S. A., Horne, R. B., & Meredith, N. P. (2014). Three-dimensional electron radiation belt simulations using the BAS Radiation Belt Model with new diffusion models for chorus, plasmaspheric hiss, and lightning-generated whistlers. *Journal of Geophysical Research: Space Physics*, *119*, 268–289. doi: 10.1002/2013JA019281

Hiraga, R., & Omura, Y. (2020). Acceleration mechanism of radiation belt electrons through interaction with multi-subpacket chorus waves. *Earth, Planets and Space*, *72*, 21. doi: 10.1186/s40623-020-1134-3

Horne, R. B., & Thorne, R. M. (2003). Relativistic electron acceleration and precipitation during resonant interactions with whistler-mode chorus. *Geophysical Research Letters*, *30*(10), 1527. doi: 10.1029/2003GL016973

Kasahara, S., Yokota, S., Mitani, T., Asamura, K., Hirahara, M., Shibano, Y., & Takashima, T. (2018). Medium-energy particle experiments?electron analyzer

(MEP-e) for the exploration of energization and radiation in geospace (ERG) mission. *Earth, Planets and Space*, *70*, 69. doi: 10.1186/s40623-018-0847-z

Kasahara, Y., Kasaba, Y., Kojima, H., Yagitani, S., Ishisaka, K., Kumamoto, A., ... Shinohara, I. (2018). The Plasma Wave Experiment (PWE) on board the Arase (ERG) satellite. *Earth, Planets and Space*, *70*, 86. doi: 10.1186/s40623-018-0842-4

Kumamoto, A., Tsuchiya, F., Kasahara, Y., Kasaba, Y., Kojima, H., Yagitani, S., ... Obara, T. (2018). High Frequency Analyzer (HFA) of Plasma Wave Experiment (PWE) onboard the Arase spacecraft. *Earth, Planets and Space*, *70*, 82. doi: 10.1186/s40623-018-0854-0

Kurita, S., Miyoshi, Y., Kasahara, S., Yokota, S., Kasahara, Y., Matsuda, S., ... Shinohara, I. (2018). Deformation of Electron Pitch Angle Distributions Caused by Upper Band Chorus Observed by the Arase Satellite. *Geophysical Research Letters*, *45*, 7996–8004. doi: 10.1029/2018GL079104

Lakhina, G. S., Tsurutani, B. T., Verkhoglyadova, O. P., & Pickett, J. S. (2010). Pitch angle transport of electrons due to cyclotron interactions with the coherent chorus subelements. *Journal of Geophysical Research: Space Physics*, *115*, A00F15. doi: 10.1029/2009JA014885

Matsuda, S., Kasahara, Y., Kojima, H., Kasaba, Y., Yagitani, S., Ozaki, M., ... Shinohara, I. (2018). Onboard software of Plasma Wave Experiment aboard Arase: instrument management and signal processing of Waveform Capture/Onboard Frequency Analyzer. *Earth, Planets and Space*, *70*, 75. doi: 10.1186/s40623-018-0838-0

Matsuoka, A., Teramoto, M., Imajo, S., Kurita, S., Miyoshi, Y., & Shinohara, I. (2018). updated daily. The MGF instrument Level-2 spin-fit magnetic field data of Exploration of energization and Radiation in Geospace (ERG) Arase satellite, Version v01.02. ERG Science Center, Institute for Space-Earth Environmental Research, Nagoya University. doi: 10.34515/DATA.ERG-06001 Accessed 2020-11-06.

Matsuoka, A., Teramoto, M., Nomura, R., Nosé, M., Fujimoto, A., Tanaka, Y., ... Shinohara, I. (2018). The ARASE (ERG) magnetic field investigation. *Earth, Planets and Space*, *70*, 43. doi: 10.1186/s40623-018-0800-1

Miyoshi, Y., Hori, T., Shoji, M., Teramoto, M., Chang, T. F., Segawa, T., ... Shino-

hara, I. (2018). The ERG Science Center. *Earth, Planets and Space*, *70*, 96. doi: 10.1186/s40623-018-0867-8

Miyoshi, Y., Kataoka, R., Kasahara, Y., Kumamoto, A., Nagai, T., & Thomsen, M. F. (2013). High-speed solar wind with southward interplanetary magnetic field causes relativistic electron flux enhancement of the outer radiation belt via enhanced condition of whistler waves. *Geophysical Research Letters*, *40*, 4520–4525. doi: 10.1002/grl.50916

Miyoshi, Y., Morioka, A., Misawa, H., Obara, T., Nagai, T., & Kasahara, Y. (2003). Rebuilding process of the outer radiation belt during the 3 November 1993 magnetic storm: NOAA and Exos-D observations. *Journal of Geophysical Research: Space Physics*, *108*(A1), 1004. doi: 10.1029/2001JA007542

Miyoshi, Y., Oyama, S., Saito, S., Kurita, S., Fujiwara, H., Kataoka, R., ... Tsuchiya, F. (2015). Energetic electron precipitation associated with pulsating aurora: EISCAT and Van Allen Probe observations. *Journal of Geophysical Research: Space Physics*, *120*, 2754–2766. doi: 10.1002/2014JA020690

Miyoshi, Y., Saito, S., Kurita, S., Asamura, K., Hosokawa, K., Sakanoi, T., ... Blake, J. B. (2020). Relativistic Electron Microbursts as High Energy Tail of Pulsating Aurora Electrons. *Geophysical Research Letters*, *47*, e2020GL090360. doi: 10.1029/2020GL090360

Miyoshi, Y., Saito, S., Seki, K., Nishiyama, T., Kataoka, R., Asamura, K., ... Santolik, O. (2015). Relation between fine structure of energy spectra for pulsating aurora electrons and frequency spectra of whistler mode chorus waves. *Journal of Geophysical Research: Space Physics*, *120*, 7728–7736. doi: 10.1002/2015JA021562

Miyoshi, Y., Shinohara, I., Takashima, T., Asamura, K., Higashio, N., Mitani, T., ... Seki, K. (2018). Geospace exploration project ERG. *Earth, Planets and Space*, *70*, 101. doi: 10.1186/s40623-018-0862-0

Omura, Y., Furuya, N., & Summers, D. (2007). Relativistic turning acceleration of resonant electrons by coherent whistler mode waves in a dipole magnetic field. *Journal of Geophysical Research: Space Physics*, *112*, A06236. doi: 10.1029/2006JA012243

Saito, S., Miyoshi, Y., & Seki, K. (2012). Relativistic electron microbursts associated with whistler chorus rising tone elements: GEMSIS-RBW simula-

631 tions. *Journal of Geophysical Research: Space Physics*, *117*, A10206. doi:
632 10.1029/2012JA018020
633 Saito, S., Miyoshi, Y., & Seki, K. (2016). Rapid increase in relativistic electron
634 flux controlled by nonlinear phase trapping of whistler chorus elements.
635 *Journal of Geophysical Research: Space Physics*, *121*, 6573–6589. doi:
636 10.1002/2016JA022696
637 Santolík, O., Parrot, M., & Lefeuvre, F. (2003). Singular value decomposition meth-
638 ods for wave propagation analysis. *Radio Science*, *38*, 1010. doi: 10.1029/
639 2000RS002523
640 Thorne, R. M., Li, W., Ni, B., Ma, Q., Bortnik, J., Chen, L., ... Kanekal, S. G.
641 (2013). Rapid local acceleration of relativistic radiation-belt electrons by
642 magnetospheric chorus. *Nature*, *504*, 411–414. doi: 10.1038/nature12889
643 Tsurutani, B. T., & Smith, E. J. (1977). Two types of magnetospheric ELF chorus
644 and their substorm dependences. *Journal of Geophysical Research (1896-1977)*,
645 *82*(32), 5112–5128. doi: 10.1029/JA082i032p05112
646 Tu, W., Cunningham, G. S., Chen, Y., Morley, S. K., Reeves, G. D., Blake, J. B.,
647 ... Spence, H. (2014). Event-specific chorus wave and electron seed popula-
648 tion models in DREAM3D using the Van Allen Probes. *Geophysical Research*
649 *Letters*, *41*, 1359–1366. doi: 10.1002/2013GL058819
650 Virtanen, P., Gommers, R., Oliphant, T. E., Haberland, M., Reddy, T., Courna-
651 peau, D., ... Contributors, S. . . (2020). SciPy 1.0: Fundamental Algorithms
652 for Scientific Computing in Python. *Nature Methods*, *17*, 261–272. doi:
653 https://doi.org/10.1038/s41592-019-0686-2